The Pennsylvania State University

The Graduate School

# RATIONAL DESIGN PROCESS FOR GAS TURBINE EXHAUST TO SUPERCRITICAL $CO_2$ WASTE HEAT RECOVERY HEAT EXCHANGER USING TOPOLOGY OPTIMIZATION

A Thesis in

Mechanical Engineering

by

Nosherwan Adil



Submitted in Partial Fulfillment
of the Requirements
for the Degree of

Master of Science

December 2021

The thesis of Nosherwan Adil is to be reviewed and approved by the following:

Alexander S. Rattner
Dorothy Quiggle Career Development Professor, Assistant Professor of Mechanical Engineering,
Thesis Adviser

Matthew J. Rau
Assistant Professor of Mechanical Engineering

Daniel Haworth
Professor of Mechanical Engineering
Head of Graduate Programs and Professor of Mechanical Engineering

# Abstract

Advances in additive manufacturing technologies and topology optimization methodologies are enabling sophisticated novel designs for heat transfer equipment. These tools have been demonstrated for development of high-performance heat sinks considering local or component-level performance factors (*e.g.*, heat transfer per volume). To leverage such capabilities in larger-scale energy systems, structured design methodologies are needed that consider factors such as production cost, cycle-level efficiency, and pressure drop constraints at system-level rather than just component-level factors. This study seeks to develop and assess a rational approach for designing thermo-economically optimal heat exchangers for such applications. The methodology is illustrated through development of the Primary Heat Exchanger (PHX) for a supercritical carbon dioxide ($sCO_2$) power cycle recovering exhaust heat from a 10 MW-scale natural gas turbine. The proposed approach begins with a detailed thermodynamic cycle model, which is then extended to account for economic impacts of the PHX. An optimal PHX heat transfer capacity target is identified, and a high-level geometry is selected based on operating characteristics. This geometry is then divided into repeating unit cells, for which topology optimization is applied to identify high-performance heat transfer surface geometries. A key aspect of this process is that the unit cell geometries are optimized using the total PHX mass / production cost as an objective function, rather than local heat transfer and flow resistance factors. Six conventional-type (longitudinally finned tubes) PHX designs are developed for comparison, and are found to yield total masses 2.7-7.7× that of the thermo-economically optimal design. The design obtained through topology optimization with a system-level techno-economic objective function is also compared with one obtained using a local thermal-fluid performance objective function. The proposed system-level approach yields a design that only requires 0.62× the mass of locally optimized HX, indicating the value of the proposed methodology. Integrating this approach with detailed additive manufacturing costing models and experimentally validated fabrication constraints can yield a streamlined workflow for advanced HX designs for future energy systems.

# TABLE OF CONTENTS

## LIST OF FIGURES

# LIST OF TABLES

# LIST OF EQUATIONS

# Acknowledgements

I would like to thank the US Department of Energy's Office of Energy Efficiency and Renewable Energy and Siemens Corporation for support under the research project "Flexible CHP System Utilizing Improved Gas Turbine and $sCO_2$ Cycles" (ORNL SAP 3400280782). The content in this thesis is solely the responsibility of the author and does not necessarily represent the official views of the funding organizations.

I would also like to thank Dr. Alexander S. Rattner, who served as my adviser and mentor, for his insightful guidance, understanding, and warm support during my Masters studies along the way to a PhD at The Pennsylvania State University. I would also like to thank all of my current and previous research group members at the Multiscale Thermal Fluids and Energy (MTFE) Laboratory. I am grateful to Assistant Professor Dr. Matthew Rau for serving as the committee member and for his insightful suggestions for the project.

I would also like to thank my father, mother, family members, and all friends for their invaluable support for the duration of my life.

# Chapter 1

# Introduction and Literature Review

Waste heat recovery (WHR) systems are being developed for industrial processes to reduce fuel consumption, limit harmful emissions, and improve production efficiency. As the operating costs of WHR systems are relatively low, capital costs of major components significantly influence overall economics. WHR systems are often specialized, and hardware must therefore be produced at low volumes. In many WHR applications, heat is recovered from low-density exhaust gas streams with strict pressure drop allowances. The primary heat exchangers (PHXs) that recover heat from such streams, must therefore be relatively large and constructed from expensive temperature and corrosion resistant materials. PHX costs can thus account for large portions of overall system costs. These factors motivate the development of methods to guide design of PHX hardware considering system-level techno-economic factors.

The present study seeks to develop an approach to rationally design such PHXs to maximize WHR system-level techno-economic performance. This approach begins with cycle level modeling, constraint identification, and economic analyses to identify overall requirements for a PHX. A high-level geometry definition is then formed considering thermal and flow factors for the waste heat and coupling fluid streams. The geometry is then improved through topology optimization, seeking to minimize total PHX mass and capital cost, while satisfying required heat transfer capacity and pressure drop constraints. Topology optimization is an algorithmic process of material and void placement within a given design domain based on certain operating conditions and manufacturing constraints. In this study, the proposed methodology is illustrated through the design of a PHX that captures waste heat from the exhaust of a microturbine entering at 482°C and supplies it to a supercritical $CO_2$ bottoming cycle.

Topology optimization is increasingly being investigated for thermal engineering problems. However, most studies have only considered local or component-level objectives, such as maximizing heat transfer in a given volume. For WHR design applications, global criteria should also be considered, such as overall system capital cost, cycle efficiency, and impacts of pressure drop effects on coupled components.

Metal additive manufacturing (AM) enables realization of the complex and involute geometries obtained from topology optimization, and therefore pairs well with the proposed PHX design approach.

AM is approaching the level of maturity that makes it viable for production of such cost-effective WHR PHXs. AM allows the use of high-performance materials (*e.g.*, specialty stainless, titanium, or nickel alloys) that can sustain high temperatures, corrosive environments, and high pressures at low incremental cost relative to AM of more common materials. Such high-performance materials may be difficult to form in conventional HX fabrication processes (*e.g.*, fin corrugation, stamping, soldering). Another advantage of AM is its suitability to customized low-volume applications, as is common for industrial WHR systems. Conversely, the proposed PHX design approach should consider limitations of AM processes, such as maximum "overhang" angles in geometries, minimum feature sizes and wall thicknesses.

### 1.1 Prior work on topology optimization of heat transfer equipment

Topology optimization is a numerical technique initially developed for structural design applications, aimed at optimizing an objective function which usually included the maximization of stiffness or minimization of compliance [1]. Since the inception of this tool as an optimal material distribution technique using homogenized design method [2], it has been extensively applied to diverse problems involving a range of physical systems [3] such as electromechanics, acoustics, thermal fluids, etc. It is expected that it might become a compulsory design tool for many newly developed technologies such as additive manufacturing. The use of this technique for optimizing thermal systems based on conductive, convective and conjugate heat transfer is a subject of ongoing research [4].

AM coupled with topology optimization has been explored in many recent investigations seeking to develop high-performance heat transfer equipment. Haertel *et. al* [5] used a density-based topology optimization scheme to maximize the conductance (inverse of thermal resistance between the two fluids) for an air-cooled heat exchanger for a prescribed pressure drop and air-side temperature change across the heat exchanger. They found that their topology optimized designs yielded 71% more conductance per unit volume, than the conventional designs.

Lange *et. al* [6] performed related investigations, and designed a heat sink using topology optimization and parametric studies, with the objective of minimizing the temperature of a cooled component. Their topology optimization and parametric based design required 1/4$^{th}$ of the mass of a conventional heat sink.

In another study, Haertel *et. al* [7] used topology optimization to improve heat sinks, employing a two-dimensional forced convection model. In their study, the objective was to minimize the heat sink temperature for a prescribed pressure drop and fixed heat generation. A 2D heat sink model with constant heat production and a density-based topology optimization model [8] was evaluated.

Kobayashi *et. al* [9] developed a novel winglet design of a fin-and-tube heat exchanger guided by topology optimization. Their optimization problem was formulated to maximize heat extraction by winglets in a two-dimensional simplified model for low Reynolds number flows. A variety of fin pattern configurations were obtained with topology optimization, and the manufacturable fin pattern adapted from the best candidate had up to 16% higher quality factor (ratio of Colburn *j* factor to friction factor) compared with the fins with rectangular winglets pairs.

Saviers *et. al* [10] applied a topology optimization methodology for developing a prototype heat exchanger design for a $sCO_2$ power cycle recuperator. They reported a 50% reduction in pressure loss and a 10% increase in heat transfer, experimentally measured for the topology optimized heat exchanger compared to the baseline design having the same wall thickness, external space dimensions, and fluid flow routing.

Most of these studies have employed local thermal-fluid performance metrics to guide optimization, such as heat transfer per volume or quality factor. However, designs that optimize such metrics may not necessarily perform best on system-level factors relevant to WHR applications, such as cycle-level efficiency or economics (*e.g.*, net present value). The approach proposed here is distinct in that the initial analytic sizing and topology optimization stages target system-level economic criteria. The methodology is illustrated here for WHR via a $sCO_2$ power cycle, but could be applicable to diverse end uses.

## 1.2 Overview of $sCO_2$ power cycle and application

Supercritical $CO_2$ power cycles have similar cycle-level working principles to closed-loop Brayton cycles, but can employ comparatively compact hardware due to the high fluid density at the 10 – 30 MPa working pressures. These cycles can achieve high thermal efficiency at relatively low turbine inlet temperatures (450°C – 750°C) because they have the advantages of both Brayton cycles, with high specific turbine work and effective recuperation, and Rankine cycles, with low compression back-work at near-critical conditions [11]. $CO_2$ is non-toxic, environmentally benign, and has favorable heat and mass transport properties. The global warming potential of $CO_2$ is 1,000 – 3,000× lower than other hydrocarbons or HFC working fluids [12]. Supercritical $CO_2$ can also effectively capture waste heat from sources with temperature glides, such as turbine exhaust or other gases. Perceived challenges to commercializing $sCO_2$ cycles include relatively high operating pressures and temperatures [13]. For these reasons, $sCO_2$ power cycles have been the subject of intense research and development efforts in recent years.

A variety of different $sCO_2$ Brayton power cycle configurations have been proposed [14], including simple recuperated cycles, recompression cycles, recompression with intercooling, recompression with partial cooling, and recompression with main-compressor intercooling. For the purposes of illustrating the PHX design process here, a simple recuperated $sCO_2$ power cycle is assumed sized for WHR from a representative ~10 MW gas turbine, as may be used in campus- or industrial-scale power generation.

# Chapter 2

# Design Methodology

## 2.1 System-level analysis and identification of design constraints and objectives

The proposed HX design process begins with a system level-model of the power generation cycle. Here, a simple recuperated $sCO_2$ power cycle is assumed with typical turbomachinery performance levels ($\eta_{comp} = \eta_{turb} = 70\%$), heat rejection to the ambient with a compressor inlet temperature of 40°C, effective recuperation ($\varepsilon_{RHX} = 0.9$), and a counterflow PHX as shown in Figure 2-1. The gas turbine exhaust gas enters the PHX at 755 K (482°C). A maximum gas turbine back pressure allowance of 4000 Pa is assumed. Based on these assumptions, the $sCO_2$ power cycle has four main degrees-of-freedom in design and operating conditions: (1) low-side pressure ($P_L$), (2) high-side pressure ($P_H$), (3) $sCO_2$ circulation rate ($\dot{m}_{CO2}$), and (4) primary heat exchanger capacity ($UA_{PHX}$) – *the component under design*.

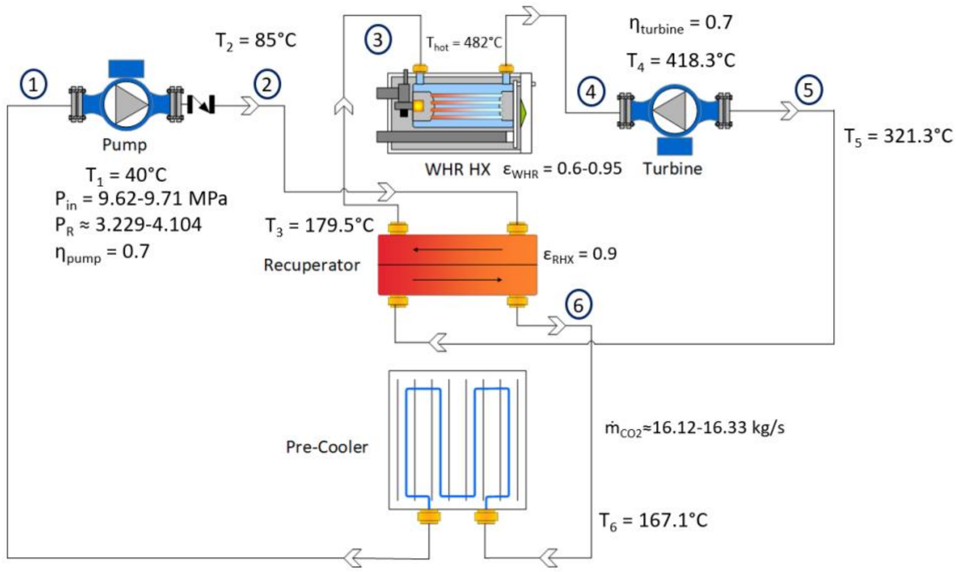


**Figure 2-1:** Cycle model for a single-stage $sCO_2$ power cycle recovering gas turbine exhaust heat

For this $sCO_2$ power cycle, optimal values of parameters 1-3 can be identified for any given value of $UA_{PHX}$ to maximize power output (Figure 2-2). The PHX capital cost can be assumed to scale with $UA_{PHX}$. Therefore, this curve can be coupled with an economic model and corresponding assumptions to identify a target $UA_{PHX}$. A cost-curve model [15] is adopted for an air-cooled heat exchanger, which leads to a target $UA_{PHX} = 225$ kW $K^{-1}$ (Section 2.2). The corresponding optimal values for $\dot{m}_{CO2}$, $P_H$, and $T_3$ ($sCO_2$

inlet temperature to PHX) will be used in the detailed HX design. Table 2-1 summarizes resulting parameters extracted from the $sCO_2$ cycle model to be used in the PHX design.

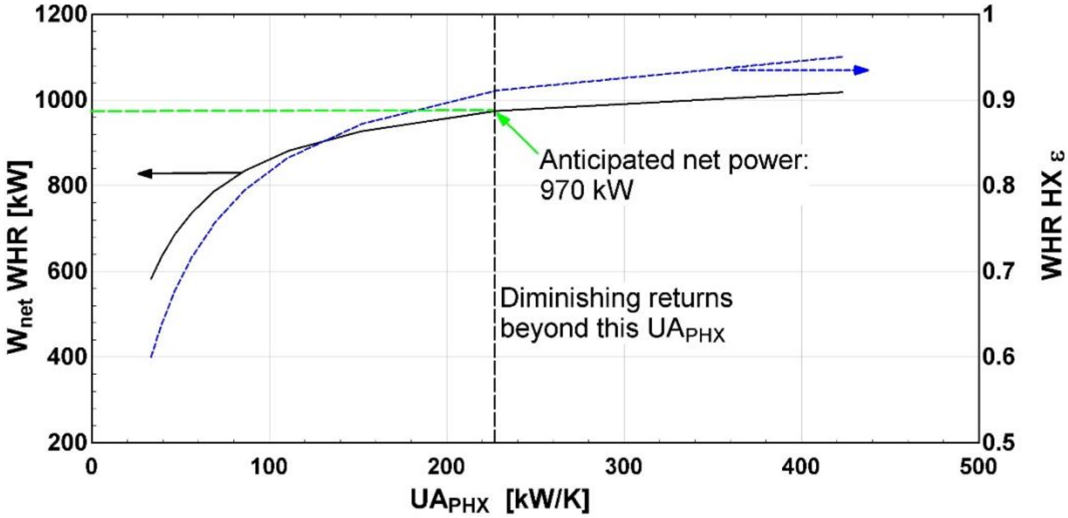


**Figure 2-2:** Maximum sCO2 cycle power output vs. PHX capacity ($UA_{PHX}$). Values for low-side pressure ($P_L$), high-side pressure ($P_H$), and $sCO_2$ mass flow rate are varied for each UA value to maximize power output.

**Table 2-1:** PHX input parameters for design

| Parameter | Value |
|---|---|
| $CO_2$ Mass Flow Rate ($\dot{m}_{co2}$) | 16.4 kg/s |
| Exhaust Mass Flow Rate ($\dot{m}_{ex}$) | 21.1 kg/s |
| HX Effectiveness ($\varepsilon_{HX}$) | 0.88 |
| $CO_2$ Side Pressure ($P_H$) | 31 MPa |
| $CO_2$ Inlet Temperature ($T_3$) | 179.5°C |

## 2.2 Basic economic model of an air-cooled HX from standard costing methods

The cost of an air-cooled heat exchanger is estimated using standard costing methods [16] to select a target UA value for the PHX. The cost of air-cooled heat exchanger is estimated from Eqn. 2-1.

$$C_{HX} = \frac{740}{397}(B_1 + B_2 F_M F_P) F_s C_{HX}^0 \qquad \text{Eqn. 2-1}$$

Here, $C_{HX}$ is the heat exchanger cost in USD, $B_1$ and $B_2$ are constants for the equipment type, $F_M$ is the material cost factor (stainless steel assumed here), $F_P$ is the pressure factor and $C_{HX}^0$ is the estimated cost of the heat exchanger made from carbon steel operating at ambient pressure in 2001 USD. Stainless steel is selected as the HX material in this study, considering the higher operating temperature and potentially reactive exhaust gas stream. The cost obtained from Eqn. 2-1 is scaled to 2019 USD using the ratio of CEPCI for the relevant years: 2001 = 397; 2019 = 740. The base cost estimate for the carbon steel HX is given by Eqn. 2-2:

$$C_{HX}^0 = \begin{cases} 10^{\left(K_1 + K_2 logA + K_3 [logA]^2\right)}, & A < 10000 \\ \frac{A}{1000} 10^{\left(K_1 + K_2 log10000 + K_3 [log10000]^2\right)}, & A > 10000 \end{cases} \qquad \text{Eqn. 2-2}$$

Where $K_1$, $K_2$ and $K_3$ are constants for the heat exchanger type, and $A$ is the area in $m^2$, over which heat exchange occurs in the heat exchanger. The pressure factor is given by Eqn. 2-3:

$$F_P = 0.939 P^{0.04759} \qquad \text{Eqn. 2-3}$$

Where $P$ is the fluid pressure in bar. The value of all constants in the previous equations are given in Table 2-2 [16]:

**Table 2-2:** Constants for PHX cost projection

| $F_S$ | $B_1$ | $B_2$ | $F_M$ | $K_1$ | $K_2$ | $K_3$ |
|---|---|---|---|---|---|---|
| 1.7 | 0.96 | 1.21 | 2.9 | 4.0336 | 0.2341 | 0.0497 |

The values for the overall heat transfer coefficient, $U$ (UA $= U \times A$), may vary depending on working fluids and HX design specifics. Here, $U$ = 300 W m$^{-2}$ K$^{-1}$ is estimated based on data for heat exchangers operating with air and fluids with similar properties to $sCO_2$ [15].

For the purposes of this PHX design study, it is assumed that the costs and efficiencies of all other WHR system components are approximately fixed. In a final design stage, varying characteristics of such components could be propagated. Given this assumption, an Incremental Net Present Value (INPV) approach can be used to select a target PHX UA value. INPV is the net value in present terms, considering all cash inflows and outflows over the equipment lifetime, relative to a baseline plant design (subscript $b$). INPV is given by Eqn. 2-4 in USD:

$$INPV = N\left(A_e - A_{e,b}\right) - \left(C_{HX} - C_{HX,b}\right) \qquad \text{Eqn. 2-4}$$

Here, $N$ is the years of lifetime (assumed 10 years in this study). $A_e$ is the electricity value produced per year in USD for a specific PHX UA, and $A_{e,b}$ is the electricity value produced per year in USD for a plant with an arbitrary baseline PHX UA (100 kW K$^{-1}$). Similarly, $C_{HX}$ and $C_{HX,b}$ are the capital costs for plants with PHXs at specific and baseline UA values, respectively. The WHR plant is assumed to operate for 8,760 hours each year, and the value of electricity is assumed to be 0.102 USD kW$^{-1}$ h$^{-1}$. The optimal PHX UA value that maximizes INPV is 225 kW K$^{-1}$ as evident from Figure 2-3. This value therefore imposes an overall component design constraint in the next steps.

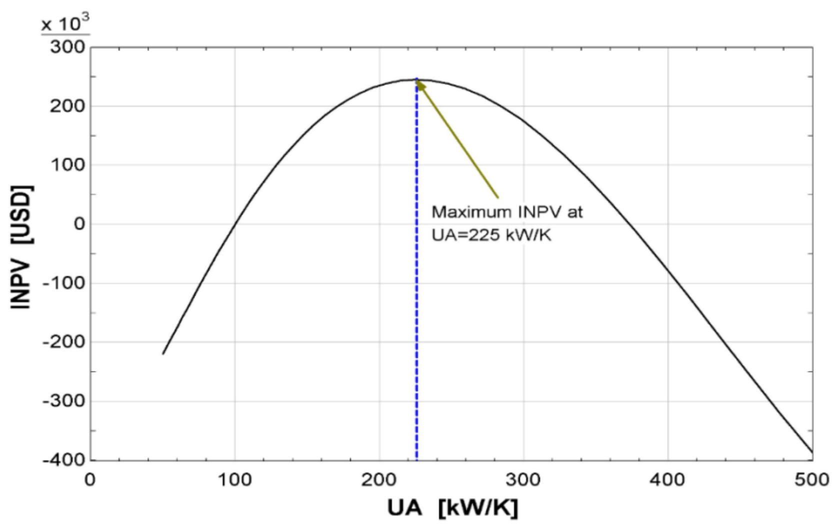


**Figure 2-3:** Incremental net present value (INPV) of WHR cycle vs. PHX UA

It should be noted that the HX design obtained through the proposed process may be unconventional, and may not conform to the assumed costing curve (Eqns. 2-1, 2-2, 2-3). Therefore, the overall design approach may be iterative in the sense that this cycle-level thermo-economic stage could be updated based on the final PHX specifications, and subsequent design steps could be repeated.

## 2.3 Formulation of design problem for topology optimization

In the counterflow PHX application, the exhaust gas volume flow rate is greater than that of the $sCO_2$ stream by ~800×. The exhaust gas pressure drop constraint is relatively low to ensure proper gas turbine operation ($\Delta P_{max} < 4{,}000$ Pa). Thus, a high performing PHX design should have much greater exhaust-side flow area than $sCO_2$ flow area. In actuality, there may be a range of acceptable $\Delta P$ values that would incur tradeoffs between the gas turbine and WHR cycles, but a single value is assumed here to streamline the design process for purpose of illustration.

Conceptually, minimizing thermal resistance between the two streams may be achieved by limiting the heat transfer distance between material elements of the two streams through any HX cross-section. From a geometric perspective, this motivates a design with circular unit-cells with a small $CO_2$ channel in the core and exhaust gas flow in the annulus. In this PHX design, such circular unit cells are reduced to hexagons, for 100% packing density in the HX cross-section, reducing component size and mass. Circular unit cells would be separated by inactive gaps of 9% area. Designs can be further constrained by assuming 12-way radial symmetry in each hexagonal unit cell (triangular sub-unit-cells, SUC). For this WHR application, the design problem reduces to optimizing the geometry of a repeating triangular SUC (Figure-2-4).

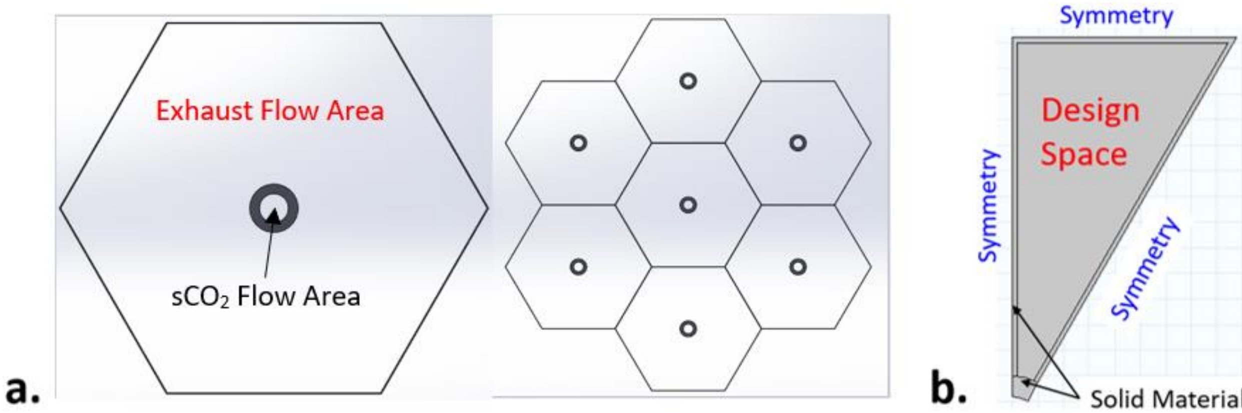


**Figure 2-4: a.** Illustrative single hexagonal unit cell (UC), which can be fully tessellated to include thousands of UCs in the HX cross-section, **b.** Sub-unit-cell (SUC) for topology optimization, with 12-way symmetry in the hexagon

For some SUC finned surface geometry (assumed prismatic for now), the number of UCs patterned in the transverse plane ($N_T$) and length in the flow direction ($L_{HX}$) can be solved to satisfy the overall PHX UA and $\Delta P$ constraints.

Given the strict pressure drop requirement, relatively small anticipated unit cells, and assumed prismatic fin geometry (*i.e.*, identical in any transverse cross-section), the exhaust flow can be assumed laminar and fully developed. For these conditions, frictional pressure drop increases linearly with flow rate and overall exhaust and fin side conductance is independent of flow rate. Therefore, each 2D fin geometry has performance constants for SUC exhaust-side flow resistance $(\nabla P/\dot{m})_{ex,SUC}$ and heat transfer capacity per length $(UA/L)_{ex,SUC}$. These constants are determined from finite element conjugate heat transfer (CHT) implemented in a customized workflow in COMSOL [17]. ($(\nabla P/\dot{m})_{ex,SUC}$, $(UA/L)_{ex,SUC}$) can be used to determine the number of unit cells in the transverse plane and streamwise length ($N_T$, $L_{HX}$) needed to satisfy overall $UA_{PHX}$ and $\Delta P_{max}$ constraints. These, in turn, determine the overall PHX mass ($M_{HX} = N_T \times L_{HX} \times (M_{UC}/L)$), which is the objective function to minimize. Here, $(M_{UC}/L)$ is the mass of a single hexagonal UC per length.

It is argued that the minimum total mass design will be the most economical to produce by additive manufacturing. A more detailed costing model could be substituted in the future that accounts for specific factors of AM processes. For example, in power-bed fusion AM, borders of parts are often formed separately and at different speeds than internal solid zones. Build costs may also be greater for vertical height than for in-plane dimensions. Perimeter length and aspect ratio factors could therefore be included for estimating fabrication costs of different geometries in more detailed formulations.

In the next phase of the design process, topology optimization is used to identify an optimal PHX SUC design. Figure 2-5 provides an overview of the proposed topology optimization process.

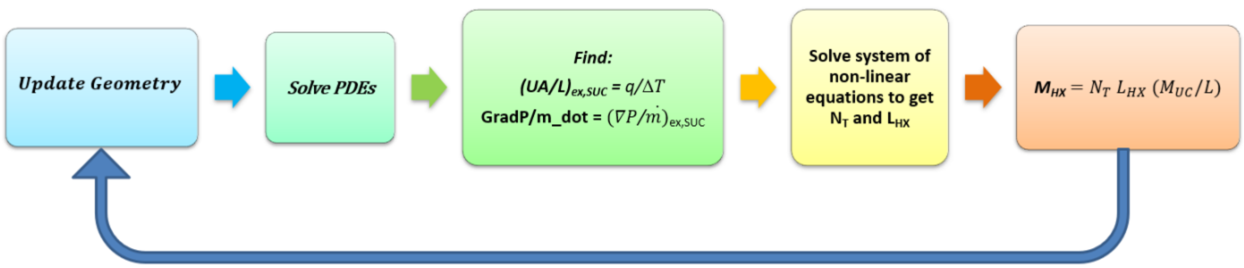


**Figure 2-5:** Flowchart for the optimization calculation procedure

A distinct aspect of this design process is that the total PHX mass (or production cost) is the objective function for topology optimization, even though geometry optimization and CHT simulations are performed at the SUC-level. If instead, optimization was performed using a local objective function based on thermal-fluid performance parameters, such as $UA_{SUC}/M_{SUC}$ or $UA_{SUC}/(\nabla P/\dot{m})_{SUC}$, resulting designs may not be economically optimal.

# Chapter 3

# Topology Optimization

### 3.1 Topology optimization problem formulation and evaluation

Topology optimization is used to converge on fin geometries in the exhaust-gas channels of the SUCs that minimize total PHX mass while satisfying UA and pressure drop constraints. To initialize the process, the edge-to-edge hexagonal UC size is assumed to be 7 mm. The inner tube diameter (ID) is chosen to be 500 μm with an outer diameter (OD) of 1,500 μm. The choice of 500 μm thickness for the $sCO_2$ circular tube is made considering the high internal pressure and minimum wall thickness requirements of typical AM systems needed to avoid porosity. Exhaust-gas side fins are allowed to be thinner as minor porosity in those structures would not lead to PHX failure. A fixed radial fin of 300 μm thickness is included in each SUC for structural integrity of the overall PHX. The choice of the 7 mm unit cell size and single fixed fin are justified through parametric studies in Sections 3.7 and 3.9, respectively. To reduce the computational cost and problem complexity, a 1/12$^{th}$ symmetric SUC is extracted from each hexagonal UC. These choices lead to a wedge-shaped *design domain* in which the exhaust-gas-side heat transfer surfaces and flow areas can be freely varied through the topology optimization calculations (Figure 3-1).

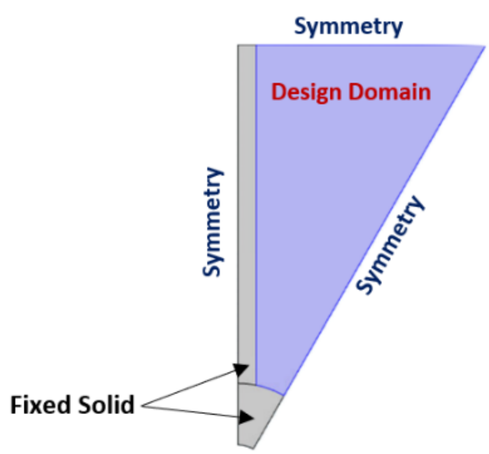


**Figure 3-1:** 1/12$^{th}$ sector sub-unit cell domain

### 3.4.1 Exhaust-gas-side flow modeling

The exhaust flow is assumed to be steady, laminar, incompressible and locally fully-developed. The laminar flow assumption is justified based on the geometry of the final optimized HX UC, which has a hydraulic diameter $D_H$ = 1.08 mm and $L_{HX}/D_H$ = 190. This corresponds to exhaust-gas Reynolds numbers ($Re_{ex}$) of 272 – 381 (varying with temperature along the flow length), which are within the laminar flow range. The locally fully-developed flow approximation is justified because the predicted laminar entrance length ($L_{ent} = 0.06 \times Re_{ex} \times D_H$) of 17 – 25 mm is approximately 10% of the total HX length of 200 mm. It should be noted that the exhaust flow properties will vary with temperature along the PHX length (~500°C – ~200°C). For laminar fully developed flow, UA and friction factor would only be modified by variations in gas conductivity and viscosity, which scale as $\sim T^{1/2}$ (~28% variation). The lower inlet density (at 482°C) is used to conservatively calculate total pressure drop. Flow blockage by the heat transfer fins is modeled with a porous media approach. To implement this effect, a Brinkman friction term is added, which imposes a resistive force proportional to velocity in solid areas, resulting in minimal penetration, as described in [18]. The resulting reduced momentum equation for pressure-driven flow in the streamwise direction is linear and given by Eqn. 3-1.

$$\mu_{ex} \nabla \cdot (\nabla \cdot w_{ex}) = \frac{\Delta P}{L_{HX}} - \bar{\alpha}(1-\gamma) w_{ex} \qquad \text{Eqn. 3-1}$$

Here, $w_{ex}$ is the exhaust gas streamwise velocity field, $\mu_{ex}$ is the exhaust gas viscosity, and $\frac{dP}{dz}$ is the uniform pressure gradient in the flow direction. $\bar{\alpha}$ is an absorption coefficient (inverse permeability) used to scale the Brinkman flow resistance term in solid zones. $\gamma$ is the design variable field generated by the iterative topology optimization process, which varies from 0 to 1 in solid and fluid regions, respectively. Ideally, the $\gamma$ field should be *sharp*, with zones of 0 (solid) and 1 (fluid) value separated by very thin transitions. However, intermediate iterations from the topology optimization algorithm may have diffuse $\gamma$ fields.

A non-dimensional form of Eqn. 3-1 is given by Eqn. 3-2.

$$\left(\frac{\partial^2 w_{ex}^*}{\partial x^{*2}} + \frac{\partial^2 w_{ex}^*}{\partial y^{*2}}\right) = \frac{dP^*}{dz^*} - \overline{\alpha^*}(1-\gamma) w_{ex}^* \qquad \text{Eqn. 3-2}$$

Here, $w_{ex}^*$ is the non-dimensional exhaust velocity defined as $\frac{w_{ex}}{U}$, where $U$ is a characteristic velocity. Similarly, $x^*$, $y^*$, and $z^*$ are non-dimensional spatial variables defined as $\frac{x}{L}$, $\frac{y}{L}$, and $\frac{z}{L}$, respectively, with characteristic length L. Moreover, $P^* = \frac{P-P_\infty}{\frac{\mu_{ex}U}{L}}$ is the dimensionless pressure with characteristic pressure $P_\infty$. $\overline{\alpha^*}$ is the dimensionless inverse permeability defined as $\frac{L^2\bar{\alpha}}{\mu_{ex}}$. The maximum inverse permeability should be sufficiently large to ensure negligible flow through solid areas, but excessively large values can cause numerical instabilities. Using the non-dimensional scaling in Eqn. 6, $\bar{\alpha}$ is chosen to be $500 \times \frac{\Delta P_{max} L}{\mu_{ex} U}$, where the characteristic length $L$ and velocity $U$ are taken as 25 mm and 1 m $s^{-1}$, respectively.

The governing flow equation (3-2) is solved for the *design domain* portion of the SUC (Figure 3-1) – the portion through which exhaust gas flows. No-slip boundary conditions are imposed on the fixed radial fin and central tube boundaries. The other SUC boundaries are symmetry planes.

Eqn. 3-2 is solved with average exhaust-gas material properties ($\mu_{ex}$ = 3.4 × $10^{-5}$ kg $m^{-1}$ $s^{-1}$, $\rho_{ex}$ = 0.48- kg $m^{-3}$) and an arbitrary pressure gradient. The total mass flow rate is then integrated over the SUC ($\dot{m}_{ex,SUC}$). As the exhaust flow is assumed laminar and fully developed, the frictional pressure gradient is linearly proportional to the mass flow in each SUC. Therefore, a characteristic flow-resistance constant can be defined for the exhaust gas flow through the SUC geometry. The characteristic $\left(\frac{\nabla P}{\dot{m}}\right)_{ex,SUC}$ constant can then be used as one of the closure parameters to solve for the PHX flow length and number of unit cells ($L_{HX}$, $N_T$) to satisfy the total pressure drop constraint as given in Section 3.4.3, Eqn. 3-16.

### 3.4.2 Exhaust-gas-side heat transfer modeling

The thermal transport equation for steady laminar flow in the axial direction is given by Eqn. 3-3:

$$\rho_{ex} C_{p,ex}\, w_{ex} \left(\frac{\partial T_{ex}}{\partial z}\right) = k_{ex} \left(\frac{\partial^2 T_{ex}}{\partial x^2} + \frac{\partial^2 T_{ex}}{\partial y^2} + \frac{\partial^2 T_{ex}}{\partial z^2}\right) + \Phi \qquad \text{Eqn. 3-3}$$

Here, $C_{p,ex}$ is the exhaust specific heat at constant pressure, $T_{ex}$ is the exhaust temperature, $k_{ex}$ is the exhaust thermal conductivity, and $\Phi$ is the volumetric viscous dissipation rate. As the exhaust gas has $Pr \sim 1$ (Pr = 0.696 at exhaust inlet temperature 482ºC), the hydrodynamically fully developed flow condition (Section 2.4.1) implies thermally developed flow. Further, the PHX operates in counterflow with nearly balanced thermal capacity rates ($\dot{m}C_p$) for both streams. Given these conditions, the exhaust gas temperature varies linearly in the flow direction, and $\frac{\partial T_{ex}}{\partial z}$ is a constant. The exhaust side Peclet number defined as the product of Reynolds number and Prandtl number ($Re_{ex} \times Pr_{ex}$) comes out to be in the range of 189-265, which is much greater than one, and hence, the second order axial conduction term ($\frac{\partial^2 T_{ex}}{\partial z^2}$) can be assumed negligible compared to the planar ones ($\frac{\partial^2 T_{ex}}{\partial x^2}, \frac{\partial^2 T_{ex}}{\partial y^2}$). The axial conduction term can also be neglected for the solid fins since $k_s/k_{ex}$=566>25 as per the criteria justified by [19] which makes the planar conduction so strong that the axial effect becomes negligible. Here, $k_s$ is the solid thermal conductivity. The non-dimensional form of the thermal transport equation is given by Eqn. 3-4:

$$w_{ex}^* \left(\frac{dT_{ex}^*}{dz^*}\right) = \frac{1}{Pe}\left(\frac{\partial^2 T_{ex}^*}{\partial x^{*2}} + \frac{\partial^2 T_{ex}^*}{\partial y^{*2}}\right) + \frac{Ec}{Re}\Phi^* \qquad \text{Eqn. 3-4}$$

Where $T_{ex}^*$ is the non-dimensional exhaust side temperature defined as $\frac{T_{ex}-T_o}{\Delta T}$, where $T_o$ and $\Delta T$ are a reference temperature and reference temperature difference, respectively. $\Phi^*$ is the dimensionless volumetric viscous dissipation rate taken as $\frac{\Phi L^2}{U^2 \mu_{ex}}$. Pe is the Peclet number which is the ratio of convective to conductive heat transport defined as $Re \times Pr = \frac{\rho_{ex} U L}{\mu_{ex}} \times \frac{C_{p,ex}\mu_{ex}}{k_{ex}}$. Ec is the Eckert number defined as $\frac{U^2}{C_{p,ex}\, \Delta T}$, which is the ratio of flow's kinetic energy to representative enthalpy difference. $Re = \frac{\rho_{ex} U L}{\mu_{ex}}$ is the Reynolds number. The ratio of Eckert number to Reynolds number $\frac{Ec}{Re}$ next to $\Phi$ is quite small in this analysis and the significance of viscous dissipation term becomes negligible as compared to other terms and hence, it can be disregarded.

The density-based topology optimization method yields a smooth variation between solid and fluid regions. The thermal conductivity field must vary correspondingly while maintaining numerical stability. Thermal conductivity is interpolated using a Rational Approximation of Material Properties (RAMP)-style function as presented in [20] and given by Eqn. 3-5:

$$k(\gamma) = k_{ex} \frac{\gamma\left(\frac{k_{ex}}{k_s}(1+b_k)-1\right)+1}{\frac{k_{ex}}{k_s}(1+b_k\gamma)} \qquad \text{Eqn. 3-5}$$

Here $k(\gamma)$ is the RAMP-style thermal conductivity, and $b_k$ is the convexity interpolation parameter that controls the convexity of the interpolation and can be adjusted to penalize intermediate design variables with respect to effective thermal conductivity. The value of $k_{ex}$, $k_s$, and $b_k$ are taken as 0.053 W $m^{-1}$ $K^{-1}$, 30 W $m^{-1}$ $K^{-1}$, and 0, respectively. The RAMP style function is selected here, instead of the Solid Isotropic Material with Penalization (SIMP) or power law forms, because it has a non-zero gradient at $\gamma = 0$. This has been found to improve convergence properties and alleviate issues with spurious low density modes in thermofluidic problems [21]. Substituting Eqn. 3-5 into Eqn. 3-4 and neglecting the viscous dissipation term, the final thermal convection diffusion equation for the current study is given by Eqn. 3-6

$$w_{ex}^*\left(\frac{dT_{ex}^*}{dz^*}\right) = \frac{1}{Pe(\gamma)}\left(\frac{\partial^2 T_{ex}^*}{\partial x^{*2}} + \frac{\partial^2 T_{ex}^*}{\partial y^{*2}}\right) \qquad \text{Eqn. 3-6}$$

Here, $Pe(\gamma) = Re \times Pr(\gamma)$, where $Pr(\gamma) = \frac{c_{p,ex}\mu_{ex}}{k(\gamma)}$. The $sCO_2$ flow travels through a circular tube, and can therefore be modeled using analytic convection correlations for fully developed turbulent channel flow as explained in the next section. The temperature of the inner tube wall is set to an arbitrary fixed value. Symmetry conditions are applied on the other SUC boundaries.

### 3.4.3 $sCO_2$ side modeling and design parameters calculation

The $sCO_2$ flows through circular channels, allowing use of analytic correlations to predict thermal resistance. Eqns. 3-7 and 3-8 are used to solve for the Reynolds number of the $sCO_2$ flow inside the tube.

$$A_{CO_2,tube} = \frac{\pi\, ID^2}{4} \qquad \text{Eqn. 3-7}$$

$$Re_{CO_2} = \frac{\mathrm{ID}\left(\frac{\dot{m}_{CO_2}}{N_T A_{CO_2,tube}}\right)}{\mu_{CO_2}} \qquad \text{Eqn. 3-8}$$

Here, $A_{\mathrm{CO_2},tube}$ is the $sCO_2$ tube cross-sectional area, $Re_{CO_2}$ is the $sCO_2$ side Reynolds number (~18,000), which is in the turbulent flow region, and $\mu_{\mathrm{CO_2}}$ is the $sCO_2$ dynamic viscosity ($3 \times 10^{-5}$ kg $m^{-1}$ $s^{-1}$). For fully developed (hydrodynamically and thermally) turbulent flow in a smooth circular tube, the local Nusselt number can be obtained from conventional channel flow correlations, such as the Dittus-Boelter equation given by Eqn. 3-9:

$$\mathrm{Nu}_{CO_2} = 0.023\ \mathrm{Re}_{CO_2}^{4/5}\ \mathrm{Pr}_{\mathrm{CO_2}}^{2/5} \qquad \text{Eqn. 3-9}$$

Here, $Nu_{CO_2}$ is the $sCO_2$ Nusselt number, and $Pr_{CO2} = 0.724$ is the $sCO_2$ side Prandtl number calculated at $T_3$ and $P_H$. The Nusselt number is then used to calculate the heat transfer coefficient and thermal resistance for the $sCO_2$ side as given by Eqns. 3-10 and 3-11, respectively:

$$HTC_{CO_2} = \frac{\mathrm{Nu}_{CO_2} k_{CO_2}}{ID} \qquad \text{Eqn. 3-10}$$

$$R_{CO_2} = \frac{1}{L_{HX} \pi ID N_T HTC_{CO_2}} \qquad \text{Eqn. 3-11}$$

Here, $HTC_{CO_2}$ is the heat transfer coefficient of the $sCO_2$ side, $k_{CO_2}$ is the thermal conductivity of $sCO_2$ (0.045 W $m^{-1}$ $K^{-1}$), and $R_{CO_2}$ is the $sCO_2$ side thermal resistance. Darcy-Weisbach and the Colebrook equations [22] are used to calculate the pressure drop and turbulent friction factor on the $sCO_2$ side as given by Eqns. 3-12 and 3-13, respectively:

$$\Delta P_{CO_2} = f \frac{L_{HX}}{ID} \frac{\dot{m}_{CO_2}}{\rho_{CO_2} N_T A_{CO_2,tube}} \qquad \text{Eqn. 3-12}$$

$$\frac{1}{\sqrt{f}} = -2log\left(\frac{\frac{\varepsilon_{abs}}{ID}}{3.7} + \frac{2.51}{Re_{CO_2}\sqrt{f}}\right) \qquad \text{Eqn. 3-13}$$

Where, $\Delta P_{CO_2}$ is the sCO$_2$ side pressure drop, $f$ is the friction factor, $\varepsilon_{abs}$ is the absolute roughness, and $\rho_{\mathrm{CO_2}} = 260\ kg\ m^{-3}$ is the sCO$_2$ side density at $T_3$ and $P_H$. Using the above correlations, the sCO$_2$ side pressure drop for the final design comes out to be ~55 kPa which is only 0.2% of the sCO$_2$ inlet pressure ($P_H$ = 31 MPa). This confirms that the sCO2-side frictional pressure drop is not an important consideration in PHX design.

Eqns. 3-8—3-13 and 3-14—3-16 are then simultaneously solved to find the PHX length ($L_{HX}$) and number of unit cells in the transverse plane ($N_T$). These parameters enable calculation of total PHX mass for a given UC geometry.

$$R_{cond,ex} = \frac{1}{12 L_{HX} N_T (UA/L)_{ex,SUC}} \qquad \text{Eqn. 3-14}$$

$$UA_{PHX} = \frac{1}{R_{\mathrm{CO_2}} + R_{cond,ex}} \qquad \text{Eqn. 3-15}$$

$$\Delta P_{ex} = \frac{\left(\frac{\nabla P}{\dot{m}}\right)_{ex,SUC} L_{HX} \dot{m}_{ex,SUC}}{12 N_T} \qquad \text{Eqn. 3-16}$$

Here, $R_{cond,ex}$ is the combined tube wall and exhaust flow resistance, $U_{PHX}$ is the UA of the PHX obtained through topology optimization, and $\Delta P_{ex}$ is the exhaust side pressure drop.

### 3.4.4 Topology optimization process

The objective function to minimize is the total PHX mass calculated from Eqns. 3-17 and 3-18:

$$\frac{M_{UC}}{L} = 12 \rho_s A_{s,SUC} \qquad \text{Eqn. 3-17}$$

$$M_{HX} = N_T L_{HX} \left(\frac{M_{UC}}{L}\right) \qquad \text{Eqn. 3-18}$$

**Objective function**

$$Minimize:\ M_{HX}$$

Here, $A_{s,UC}$ is the total solid area in the SUC, $\rho_s = 7500 \text{ kg m}^{-3}$ (stainless steel) is the solid density, and $M_{HX}$ is the final mass of the heat exchanger.

SUC geometries are obtained using the COMSOL density-based topology optimization module [23]. For such poorly conditioned thermal fluid problems, the optimization module uses a Helmholtz filter [24] that imposes a minimum length scale on a domain control design variable. Eqn. 3-19 provides the filtering equation:

$$\gamma_f = R_{min}^2 \nabla^2 \gamma_f + \gamma_c \qquad \text{Eqn. 3-19}$$

Here, $R_{min}$ is the minimum length scale, $\gamma_f$ is the filtered design variable, and $\gamma_c$ is the control design variable. The mesh element size is taken as the default filter radius and $\gamma_f$ is continuous and discretized with linear polynomials.

The filtered design variable can have areas with intermediate values, resulting in an unphysical geometry. A hyperbolic tangent projection function [8] is used to sharpen the design variable field given by Eqn. 3-20:

$$\gamma = \frac{(\tanh\left(\beta(\gamma_f - \gamma_\beta)\right) + \tanh(\beta\gamma_\beta))}{(\tanh\left(\beta(1 - \gamma_\beta)\right) + \tanh(\beta\gamma_\beta))} \qquad \text{Eqn. 3-20}$$

Here $\gamma_\beta$ is the projection point, and $\beta$ is the projection slope. The COMSOL default values of $\gamma_\beta = 0.5$ and $\beta = 8$ are used here.

A gradient-based solver is used because it follows a path in the design variable space where each new iteration is based on local derivative information evaluated at previously visited points. The Method of Moving Asymptotes (MMA) solver is used in this study because it can handle problems of any form and is especially suitable for problems with a large number of control variables. The adjoint based gradient calculation numerical method is employed which uses checkpointing to reduce the amount of data which needs to be stored from the forward to the backward (adjoint) solution stage.

The size of features or branches obtained from this topology optimization approach depends upon the mesh resolution. To streamline computation, the optimization procedure is initiated on a triangular coarse mesh which has few degrees of freedom and quickly converges. However, the output of this stage typically has diffuse boundaries between solid and fluid zones. The mesh is iteratively refined, initialized with the converged $\gamma$ field obtained with the preceding mesh, and then solved. This process is continued until a sufficiently accurate and well-defined boundaries are achieved. Six different mesh sizes are used in this study ranging from coarser to extra fine. Figure 3-2 provides a depiction of the mesh sizes for the initial and final steps used in this study:

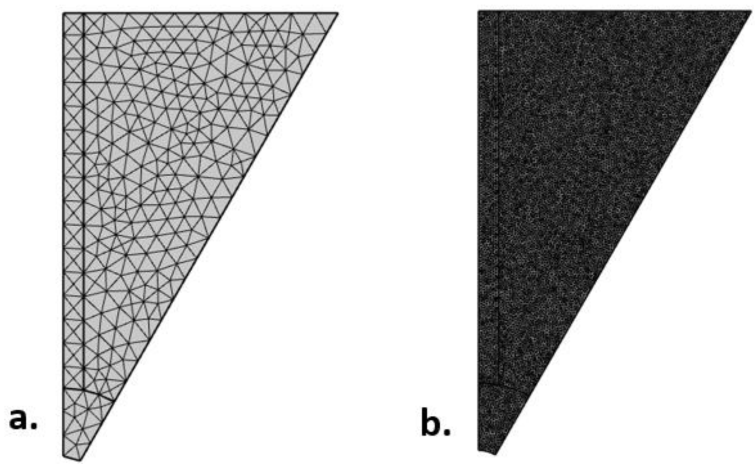


**Figure 3-2: a.** Initial mesh (element size range = 8.1 –176 μm, Degrees of Freedom (DOF) = 1,907), **b.** Final Finer Mesh (element size range = 0.3 –26.3 μm, DOF = 80,905)

### 3.5 Inexact density-based result to exact formulation

Even with mesh refinement, the density-function-based adjoint topology optimization solution can still yield diffuse boundaries near solid-gas interfaces. The design variable field ($\gamma$) may be at intermediate values (other than 0 or 1) near bulk solid and gas regions (Figure 3-3a). Therefore, the density-method based optimized solution for $\gamma$ should be treated as a guideline that requires correction.

Here, the design function field is exported from the topology optimization finite element solver (COMSOL) to a CAD program. Sharp boundaries between the solid and gas regions are manually traced (Figure 3-3b). CHT simulations are then repeated for this corrected geometry with well-defined solid and fluid regions. An extremely fine mesh is used for the concerned simulation with element sizes of 0.08 – 40-

μm to ensure well converged results (DOF = 68,948). The exhaust flow is assumed to be steady, laminar, incompressible and fully-developed as justified earlier in Section 3.4.1. Eqn. 3-21 provides the fluid dynamics modeling used in the CHT analysis and solved in the wedge-shaped subdomain in Figure 8b (shown in blue). Similarly, Eqn. 3-22 is used to solve for the temperature field.

$$\mu_{ex}\left(\frac{\partial^2 w_{ex}}{\partial x^2}+\frac{\partial^2 w_{ex}}{\partial y^2}\right)=\frac{\partial P}{\partial z} \qquad \text{Eqn. 3-21}$$

$$\rho_{ex} C_{p,ex}\, w_{ex}\left(\frac{dT_{ex}}{dz}\right)=k_{ex}\left(\frac{\partial^2 T_{ex}}{\partial x^2}+\frac{\partial^2 T_{ex}}{\partial y^2}\right) \qquad \text{Eqn. 3-22}$$

The simulations with this exact geometry provide corrected values of UC mass per length of HX ($M_{UC}/L$), fin and exhaust-side UA per length per SUC ($(UA/L)_{ex,SUC}$), and exhaust-side pressure gradient per mass flow rate per SUC $\left(\frac{\nabla P}{\dot{m}}\right)_{ex,SUC}$. Refined values of $N_T$, $L_T$, and $M_{HX}$ are then obtained using the algorithm described in Section 3.4.1-3.4.4 (Eqns. 3-14—3-18).

### 3.6 Topology optimization results

The topology-optimization result obtained for a UC size of 7 mm, total pressure drop constraint of 4 kPa, and overall PHX conductance of 225 kW K$^{-1}$ is depicted in Figure 3-4 along with its tessellation to fully hexagonal single unit cell:

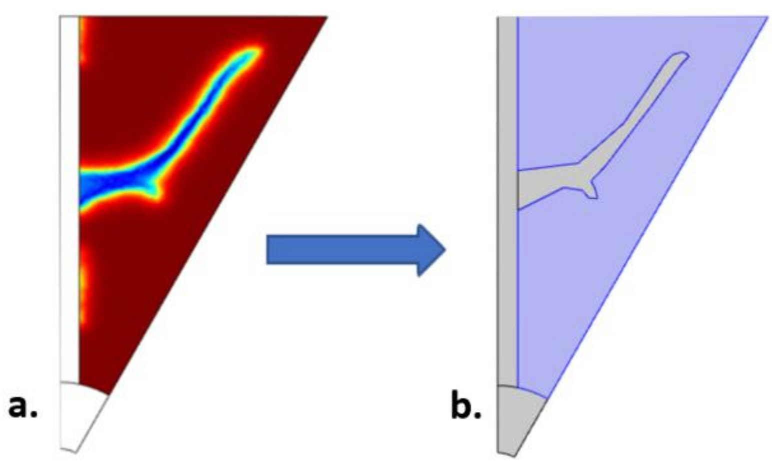


**Figure 3-3: a.** Topology based result. Red = Fluid, Blue = Porous Solid, White = Fixed Solid, **b.** Exact geometry generated in CAD software

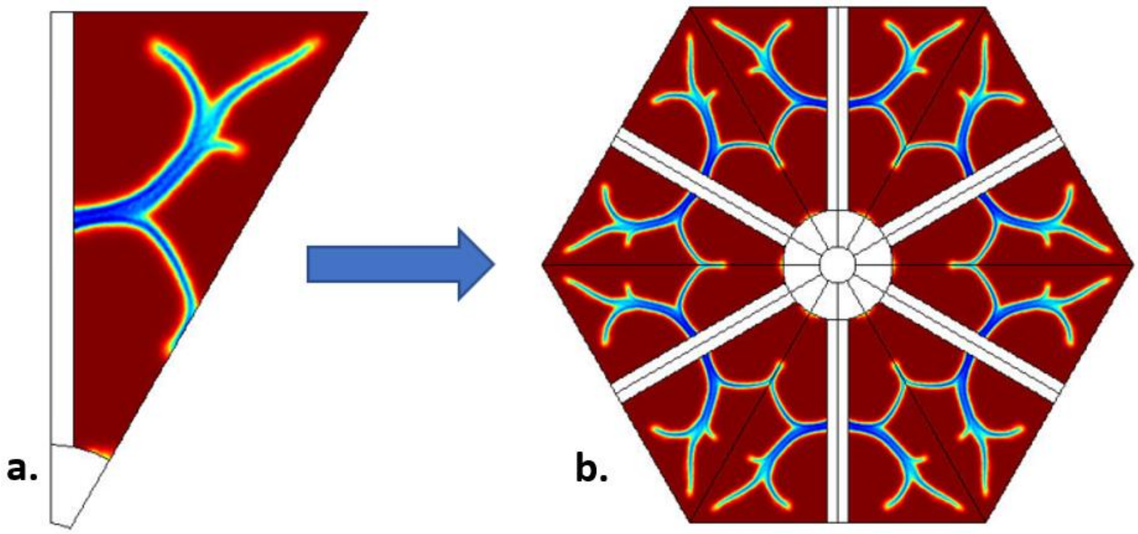


**Figure 3-4: a.** Topology based result. Red = Fluid, Blue = Porous Solid, White = Fixed Solid, **b.** Tessellation to single hexagonal UC

Figure 3-5 shows the solid portion of the hexagonal UC CAD, and an illustration of multiple connected unit cells. The full PHX may contain thousands of connected hexagonal UCs.

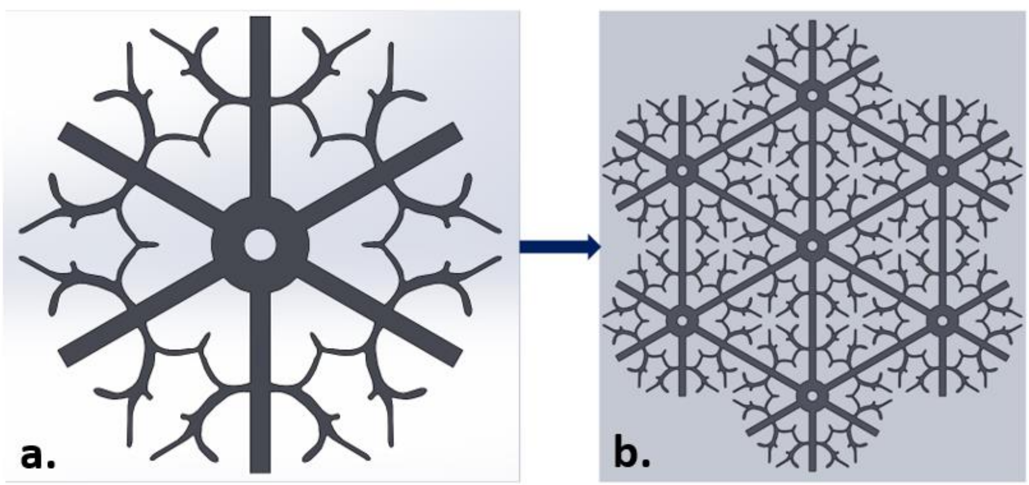


**Figure 3-5: a.** Solid Hexagonal UC, **b.** Illustration of multiple connected UCs

Using the CHT analysis and solving for the parameters as discussed in Section 2.5, the final predicted mass of a stainless steel PHX ($\rho_s$ = 7500 kg m$^{-3}$), number of UCs in the transverse cross section, length, total cross-sectional area, and UC heat transfer and flow resistance parameters are summarized in Table 3-1.

**Table 3-1:** Final PHX parameters for optimized 7 mm hexagonal unit cells

| | |
|---|---|
| **$M_{HX}$ (kg)** | 1,300 |
| **$N_T$** | 77,000 |
| **Frontal Area ($m^2$)** | 3.2 |
| **$L_{HX}$ (m)** | 0.20 |
| **$\mathbf{GradP_{\dot{m},UC}}$ (Pa s kg$^{-1}$ m$^{-1}$)** | $7.1\times10^7$ |
| **$\mathbf{(UA/L)_{ex,UC}}$ (W m$^{-1}$ K$^{-1}$)** | 14.3 |

## 3.7 Unit cell sizing analysis

The performance of the PHX employing optimized 7 mm UCs is compared with those using 6 and 8 mm UCs, generated through the same procedure. Moreover, a second comparative study is performed to assess the use of 6 fixed radial fins in the UC (baseline) vs. 12. Figure 3-6 shows a depiction of these topologically optimized SUCs. Table 3-2 provides the mass calculated by utilizing the UCs from these SUCs.

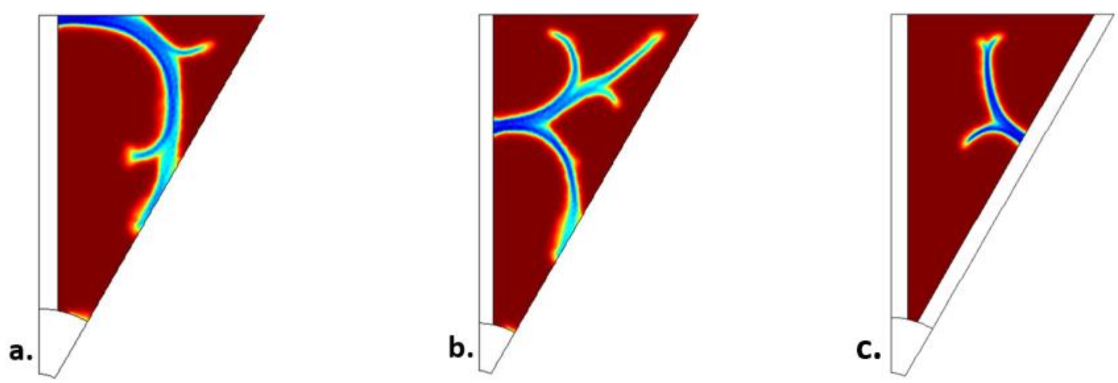


**Figure 3-6:** Topology optimization results for: **a.** 6 mm SUC (6 fixed fins UC), **b.** 8 mm SUC (6 fixed fins UC), **c.** Double radial fin (300 um) SUC from a 7 mm UC (12 fixed fins)

**Table 3-2:** UC size vs. HX parameters

| | **UC Size (mm) and fixed radial fin count** | | | |
|---|---|---|---|---|
| | **6** (6 fixed fins) | **7** (6 fixed fins) baseline | **7** (12 fixed fins) | **8** (6 fixed fins) |
| **$M_{HX}$ (kg)** | 2,000 | 1,300 | 1,600 | 1,850 |
| **$N_T$** | 100,000 | 77,000 | 78,000 | 58,000 |
| **Frontal Area ($m^2$)** | 3.3 | 3.2 | 3.3 | 3.2 |
| **$L_{HX}$ (m)** | 0.30 | 0.20 | 0.20 | 0.36 |
| **$GradP_{\dot{m},UC}$ (Pa s $kg^{-1}$ $m^{-1}$)** | $6.8\times10^7$ | $7.1\times10^7$ | $7.5\times10^7$ | $3.0\times10^7$ |
| **$(UA/L)_{ex,UC}$ (W $m^{-1}$ $K^{-1}$)** | 7.0 | 14.3 | 14.7 | 10.6 |

Both the smaller (6 mm) and larger (8 mm) UCs yield greater HX mass and dimensions, suggesting that the 7 mm UC size is near-optimal. Although, the heat transfer performance $(UA/L)_{ex,UC}$ of the UC with 12 fixed fins is greater than with 6 fixed fins, the total PHX mass is 1.23x greater. This supports the selection of 6 radial fixed fins in Section 3.4 to minimize PHX mass. This also highlights the value of using cycle-level economic criteria for optimization, as greater local heat transfer intensity $(UA/L)_{ex,UC}$ does not necessarily minimize global HX mass.

### 3.8 System vs. local level topology optimization

A key contribution of this study is in the use of topology optimization objective function formulated based on system-level considerations rather than local transport parameters. To illustrate the impact of this approach, topology optimization is also performed for the baseline unit cell with the objective of maximizing heat transfer within the design domain. For fully-developed laminar flow in a SUC of given geometry, UA is independent of flow rate, frictional pressure drop and proportional to average flow velocity. Therefore, a thermal-fluid performance constant can be determined for any SUC:

$$\boldsymbol{Maximize}: \frac{UA}{\frac{\nabla P}{w_{avg}}}$$

Here, $\nabla P$ is an arbitrary driving pressure gradient taken as 4 kPa m$^{-1}$, and $w_{avg}$ is the average flow velocity through the design domain. This thermal-fluid performance factor can be obtained for a SUC following the procedures defined in Sections 3.4.1-3.4.2. Figure 3-7 presents the geometry obtained with this objective function and Table 3-3 provides the resulting PHX parameters.

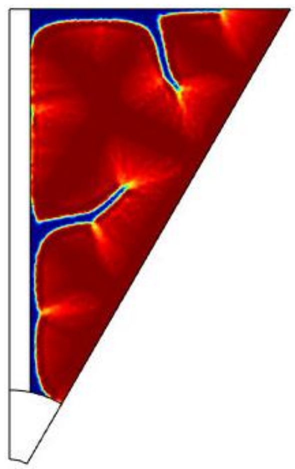

**Figure 3-7:** Topologically optimized SUC (Objective function=Local heat transfer maximization)

**Table 3-3:** Locally optimized HX parameters

| | |
|---|---|
| **$M_{HX}$ (kg)** | 2,100 |
| **$N_T$** | 63,000 |
| **Frontal Area (m$^2$)** | 2.7 |
| **$L_{HX}$ (m)** | 0.46 |
| **$GradP_{\dot{m},UC}$ (Pa s kg$^{-1}$ m$^{-1}$)** | $2.6\times10^7$ |
| **$(UA/L)_{ex,UC}$ (W m$^{-1}$ K$^{-1}$)** | 7.8 |
| **$N_T$** | 63,000 |

This locally optimized SUC has higher mass than the one in Section 3.6, but also has lower $(UA/L)_{ex,UC}$. The locally optimized HX is 1.6x massive than the globally optimized one. The $\frac{\frac{UA}{\nabla P}}{w_{avg}}$ objective function for the local and system level optimized baseline UC comes out to be 680 $dm^5\ s^{-2}\ K^{-1}$ and 460 $dm^5\ s^{-2}\ K^{-1}$. It can be seen that the higher local objective function does not necessarily result into a lower system level mass objective function. Hence, the technique in this paper stands out with its optimized system level results.

### 3.9 Conventional designs

To illustrate the potential of the proposed topology-optimization based approach, six *conventional*-type designs are also developed. These only include radial (longitudinal) fins in the 7 mm UC, which can be fabricated with conventional HX processes. The number and size of radial fins are varied in these designs. Figure 3-8 provides the two basic SUCs used for conventional designs with varying fin thickness.

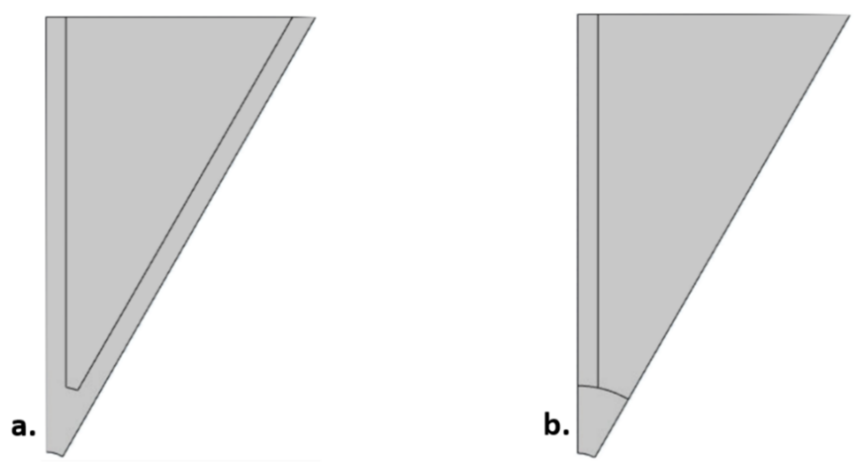


**Figure 3-8: a.** Double Longitudinal Fin SUC (Tessellates to 12-fin UC),
**b.** Single Longitudinal Fin SUC (Tessellates to 6-fin UC)

CHT computations are performed for these geometries as in Section 3.5 to solve for $M_{UC}/L$, $(UA/L)_{ex,SUC}$, and $\left(\frac{\nabla P}{\dot{m}}\right)_{ex,SUC}$. These values are used to obtain $N_T$, $L_{HX}$ and $M_{HX}$ for the required UA and pressure drop values. The respective mass values for the basic HX designs are given in Table 3-4.

**Table 3-4:** HX parameters for conventional designs

| | | **No. of fins** | | | | | |
|---|---|---|---|---|---|---|---|
| | | **6** | | | **12** | | |
| **Fin Thickness (μm)** | **300** | $N_T$ | $L_{HX}$ **(m)** | $M_{HX}$ **(kg)** | $N_T$ | $L_{HX}$ **(m)** | $M_{HX}$ **(kg)** |
| | | **52,000** | **2.70** | **6,800** | **70,000** | **0.55** | **3,500** |
| | **400** | $N_T$ | $L_{HX}$ **(m)** | $M_{HX}$ **(kg)** | $N_T$ | $L_{HX}$ **(m)** | $M_{HX}$ **(kg)** |
| | | **55,000** | **2.50** | **8,500** | **78,000** | **0.47** | **4,400** |
| | **500** | $N_T$ | $L_{HX}$ **(m)** | $M_{HX}$ **(kg)** | $N_T$ | $L_{HX}$ **(m)** | $M_{HX}$ **(kg)** |
| | | **58,000** | **2.36** | **10,000** | **90,000** | **0.41** | **5,300** |

It can be seen from Table 3-4 that the mass of conventional heat exchangers without any topology-optimization features is comparatively high. There is a trend towards lower PHX mass with reducing fin thickness, but unfeasibly thin materials may be needed to outperform the topology optimized design.

# Chapter 4

# Conclusions and Future Research Recommendations

This study presents a design process for cost effective HXs for applications including WHR systems. The approach begins with a cycle level thermodynamic model power cycle to assess the impact of PHX UA and flow resistance on system efficiency. This is then coupled to an economic model that balanced system efficiency (value of produced electricity) and capital costs to identify a target HX UA. A high-level HX geometry template is then formed, and used as a basis for topology optimization. Topology optimization is then applied using a CHT physical model and an objective function of minimizing total HX mass, a surrogate for capital cost. The resulting design achieves a 2.7-7.7x reduction in HX mass compared with simple designs employing longitudinal fins.

The technique of topology optimization applied in this paper at a global thermo-economic scale takes into account the performance of the whole system and thus produces designs for cost effective HXs. For comparison, topology optimization was performed using a local thermal-fluid performance objective function $\frac{UA}{\frac{\nabla P}{w_{avg}}}$ to design a HX with equal UA and pressure loss. The design obtained considering global thermo-economic factors requires 38% less mass.

The present investigation focuses on the development and theory of a PHX design process, but practicalities of fabrication have not yet been thoroughly studied. Future work is needed to assess production of such complex HXs using AM. A more detailed AM costing model should be developed and verified. In future work, minimum AM feature sizes and surface roughness should be considered in the CHT and topology optimization stages. AM HXs can be experimentally tested for manufacturing defects to provide data about limitation for minimum tube wall and fin thicknesses along with allowable feature sizes. They can also be evaluated for pressure drop and hydrostatic burst strength. Moreover, topology optimization can also be applied to the $sCO_2$ side which may result in an even more mass efficient heat exchanger.

## Bibliography

[1] E. M. Dede, S. N. Joshi, and F. Zhou, "Topology Optimization, Additive Layer Manufacturing, and Experimental Testing of an Air-Cooled Heat Sink," *J. Mech. Des. Trans. ASME*, 2015, doi: 10.1115/1.4030989.

[2] M. P. Bendsøe and N. Kikuchi, "Generating optimal topologies in structural design using a homogenization method," *Comput. Methods Appl. Mech. Eng.*, 1988, doi: 10.1016/0045-7825(88)90086-2.

[3] E. M. Dede, J. Lee, and T. Nomura, *Multiphysics Simulation: Electromechanical System Applications and Optimization*. 2014.

[4] T. Dbouk, "A review about the engineering design of optimal heat transfer systems using topology optimization," *Applied Thermal Engineering*. 2017, doi: 10.1016/j.applthermaleng.2016.10.134.

[5] J. H. K. Haertel and G. F. Nellis, "A fully developed flow thermofluid model for topology optimization of 3D-printed air-cooled heat exchangers," *Appl. Therm. Eng.*, 2017, doi: 10.1016/j.applthermaleng.2017.03.030.

[6] F. Lange, C. Hein, G. Li, and C. Emmelmann, "Numerical optimization of active heat sinks considering restrictions of selective laser melting," *COMSOL Conf. 2018 Lausanne*, 2018.

[7] J. Haertel, K. Engelbrecht, B. Lazarov, and O. Sigmund, "Topology Optimization of Thermal Heat Sinks," *COMSOL Conf.*, 2015.

[8] F. Wang, B. S. Lazarov, and O. Sigmund, "On projection methods, convergence and robust formulations in topology optimization," *Struct. Multidiscip. Optim.*, 2011, doi: 10.1007/s00158-010-0602-y.

[9] H. Kobayashi, K. Yaji, S. Yamasaki, and K. Fujita, “Freeform winglet design of fin-and-tube heat exchangers guided by topology optimization,” *Appl. Therm. Eng.*, 2019, doi: 10.1016/j.applthermaleng.2019.114020.

[10] K. R. Saviers, R. Ranjan, and R. Mahmoudi, “Design and validation of topology optimized heat exchangers,” 2019, doi: 10.2514/6.2019-1465.

[11] S. K. Cho, M. Kim, S. Baik, Y. Ahn, and J. I. Lee, “Investigation of the bottoming cycle for high efficiency combined cycle gas turbine system with supercritical carbon dioxide power cycle,” 2015, doi: 10.1115/GT2015-43077.

[12] K. Nikitin, Y. Kato, and L. Ngo, “Printed circuit heat exchanger thermal-hydraulic performance in supercritical CO2 experimental loop,” *Int. J. Refrig.*, 2006, doi: 10.1016/j.ijrefrig.2005.11.005.

[13] M. Persichilli, T. Held, S. Hostler, and E. Zdankiewicz, “Transforming Waste Heat to Power through Development of a CO2 - Based Power Cycle,” *16th Int. Symp. Compress. Users-Manufacturers*, 2011.

[14] C. S. Turchi, Z. Ma, T. W. Neises, and M. J. Wagner, “Thermodynamic study of advanced supercritical carbon dioxide power cycles for concentrating solar power systems,” *J. Sol. Energy Eng. Trans. ASME*, 2013, doi: 10.1115/1.4024030.

[15] A. D. Atrens, H. Gurgenci, and V. Rudolph, “Economic Optimization of a CO2-Based EGS Power Plant,” *Energy & Fuels*, vol. 25, no. 8, pp. 3765–3775, Aug. 2011, doi: 10.1021/ef200537n.

[16] R. et al. Turton, “Analysis, Synthesis, and Design of Chemical Processes, Prentice Hall International Series,” *Chem. Process Equip.*, 2001, doi: 10.1016/B978-075067510-9/50032-2.

[17] “COMSOL Multiphysics® v. 5.4.” www.comsol.com. COMSOL AB, Stockholm, Sweden.

[18] T. Borrvall and J. Petersson, “Topology optimization of fluids in Stokes flow,” *Int. J. Numer. Methods Fluids*, 2003, doi: 10.1002/fld.426.

[19] S. X. Zhang, Y. L. He, G. Lauriat, and W. Q. Tao, “Numerical studies of simultaneously developing laminar flow and heat transfer in microtubes with thick wall and constant outside wall temperature,” *Int. J. Heat Mass Transf.*, 2010, doi: 10.1016/j.ijheatmasstransfer.2010.05.017.

[20] M. Stolpe and K. Svanberg, “An alternative interpolation scheme for minimum compliance topology optimization,” *Struct. Multidiscip. Optim.*, 2001, doi: 10.1007/s001580100129.

[21] O. Sigmund and K. Maute, “Topology optimization approaches,” *Struct. Multidiscip. Optim.*, 2013, doi: 10.1007/s00158-013-0978-6.

[22] Y. Cengel and Cimbala, *Fluid Mechanics: Fundamentals and Applications, 3rd ed*. 2010.

[23] COMSOL Multiphysics, “Optimization Module,” *User’s Guid.*, 2015.

[24] B. S. Lazarov and O. Sigmund, “Filters in topology optimization based on Helmholtz-type differential equations,” *Int. J. Numer. Methods Eng.*, 2011, doi: 10.1002/nme.3072.